The Partitioning of Poleward Heat Transport between the Atmosphere and Ocean

ARNAUD CZAJA

Department of Physics, Imperial College, London, United Kingdom

JOHN MARSHALL

Department of Earth, Atmosphere and Planetary Sciences, Massachusetts Institute of Technology, Cambridge, Massachusetts

(Manuscript received 28 February 2005, in final form 28 September 2005)

ABSTRACT

Observations of the poleward heat transport of the earth (H) suggest that the atmosphere is the primary transporting agent poleward of 30°, that oceanic (H_O) and atmospheric (H_A) contributions are comparable in the tropical belt, and that ocean transport dominates in the deep Tropics.

To study the partition we express the ratio H_A/H_O as

$$\frac{H_A}{H_O} = \frac{\Psi_A}{\Psi_O} \times \frac{C_A \Delta\theta_A}{C_O \Delta\theta_O},$$

where Ψ (with subscripts A and O denoting atmosphere and ocean, respectively) is the meridional mass transport within θ layers (moist potential temperature for the atmosphere, potential temperature for the ocean), and $C\Delta\theta$ (C being the specific heat) is the change in energy across the circulation defined by Ψ.

It is argued here that the observed partitioning of heat transport between the atmosphere and ocean is a robust feature of the earth's climate and reflects two limits: (i) dominance of atmospheric mass transport in mid-to-high latitudes ($\Psi_A \gg \Psi_O$ with $C_A\Delta\theta_A \sim C_O\Delta\theta_O$ and hence $H_A/H_O \gg 1$) and (ii) dominance of oceanic energy contrast in the Tropics ($C_O\Delta\theta_O \gg C_A\Delta\theta_A$ with $\Psi_A \sim \Psi_O$ and hence $H_A/H_O \ll 1$).

Motivated by simple dynamical arguments, these ideas are illustrated through diagnosis of atmospheric reanalyses, long simulations of an ocean model, and a coupled atmosphere–ocean model of intermediate complexity.

1. Introduction

Figure 1a shows an estimate of the atmospheric (H_A, black) and oceanic (H_O, gray) heat transport from data published by Trenberth and Caron (2001), based on National Centers for Environmental Prediction (NCEP) and European Centre for Medium-Range Weather Forecasts (ECMWF) atmospheric reanalyses (continuous and dashed curves, respectively). Both atmospheric products suggest that (Fig. 1b), poleward of about 30°, the atmospheric contribution to the total poleward heat transport amounts to roughly 90% of the total. As one approaches lower latitudes, however, both contribute in roughly equal amounts, although a precise estimate is made difficult by the fact that both H_O and H_A become small in the Tropics (note the large spread between the dashed and continuous curves in Fig. 1b equatorward of 10°).

An obvious question is whether there is a simple physical explanation for the partitioning suggested in Fig. 1b. An important step toward this goal was recently made by Held (2001), who represented the oceanic and atmospheric heat transport as the product of an overturning mass transport streamfunction Ψ and an energy contrast $C\Delta\theta$,

$$H_{A,O} = \Psi_{A,O} C_{A,O} \Delta\theta_{A,O} \tag{1}$$

where the subscripts A, O denote atmospheric and oceanic values, and C and $\Delta\theta$ are, respectively, the heat capacity and difference in an appropriately defined potential temperature across the upper and lower branches of the overturning circulation (as we shall see the relevant quantity is moist static energy for the at-

Corresponding author address: Dr. Arnaud Czaja, Dept. of Physics, Imperial College, Prince Consort Road, London, SW7 2AZ, United Kingdom.
E-mail: a.czaja@imperial.ac.uk

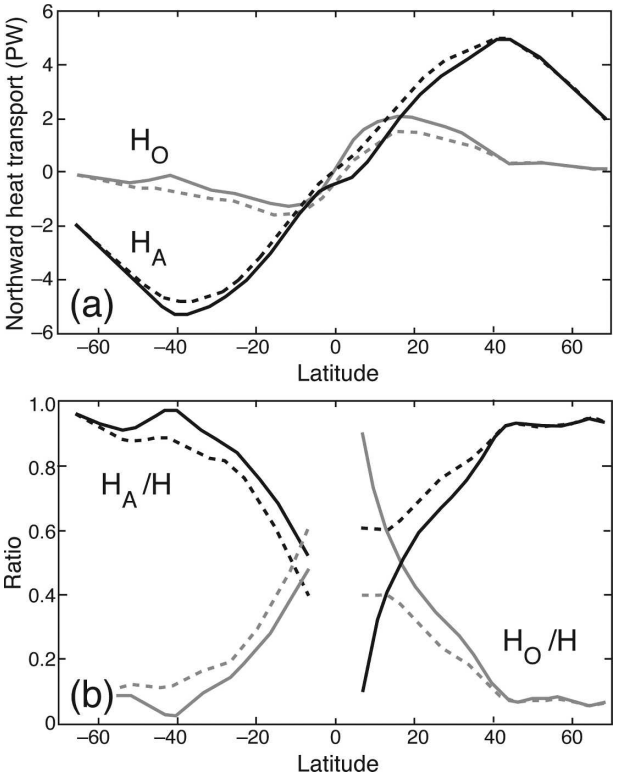

FIG. 1. (a) Estimates of oceanic (H_O, gray) and atmospheric (H_A, black) heat transport in PW (1 PW = 10^{15} W). (b) Relative contribution of ocean (gray) and atmosphere (black) to the total energy transport $H = H_O + H_A$ using (a). Continuous curves correspond to NCEP-based estimates, while dashed curves correspond to ECMWF-based estimates. The ratios in (b) were not plotted in the deep Tropics (2°S–2°N) where $H_A + H_O$ vanishes.

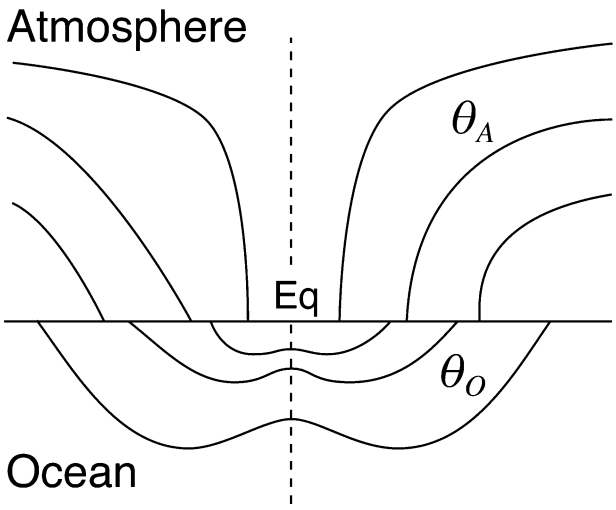

FIG. 2. Schematic of the distribution of atmospheric moist potential temperature (θ_A, i.e., moist static energy) and oceanic potential temperature (θ_O) as a function of latitude and height (black contours). The equator is indicated as a vertical dashed line.

mosphere and potential temperature referenced to the surface for the ocean). Such a decomposition is commonly carried out in oceanography (e.g., Talley 2003). Using Eq. (1), the ratio of atmospheric to oceanic heat transport becomes

$$\frac{H_A}{H_O} = \frac{\Psi_A}{\Psi_O} \times \frac{C_A \Delta\theta_A}{C_O \Delta\theta_O}. \tag{2}$$

In the Tropics, where transfer by quasi-two-dimensional atmospheric eddies is largely absent, Held (2001) argued that oceanic and atmospheric mass transports are close to one another and set by the Ekman meridional mass transport. He went on to propose that the relative magnitude of $C\Delta\theta$ in Eq. (1) must be responsible for the partitioning. To rationalize this, Held suggested that $C\Delta\theta$ is essentially a measure of the oceanic and atmospheric stratification in the Tropics. Oceanic stratification is high in the deep Tropics where upwelling of cold fluid to the warm surface on the equator forms a pronounced thermocline. In the atmosphere, by contrast, tropical deep convection acts to return the fluid to marginal stability to moist processes in which θ_A, the moist static energy, has weak vertical gradients. The state of affairs is schematized in Fig. 2. Hence, as Held (2001) emphasized, dominance of ocean heat transport over atmospheric is expected in the deep Tropics.

It is not straightforward to carry this argument to mid-to-high latitudes where it is well established that atmospheric transient eddies cannot be ignored when estimating meridional mass transports. Thus we might expect Ψ_A and Ψ_O to decouple moving away from the Tropics, and the role of stratification in setting the partitioning becomes much less clear.

In this paper, we attempt to estimate oceanic and atmospheric heat transports globally, motivated by the decomposition Eq. (1). To do so, we will estimate the meridional mass transports within potential temperature layers—defined by moist static energy in the atmosphere and potential temperature in the ocean—which will allow us to estimate Ψ and $C\Delta\theta$ directly from data. Our main conclusion is that the partitioning seen in Fig. 1b can be simply understood as two limits of Eq. (2): a mass transport "Ψ limit" in mid-to-high latitudes where $\Psi_A \gg \Psi_O$ and the atmospheric contribution to $H = H_O + H_A$ dominates; an energy contrast "$C\Delta\theta$ limit" in the Tropics where $C_A\theta_A \ll C_O\theta_O$ and where the oceanic contribution to H overwhelms that of the atmosphere.

The paper is set out as follows. Sections 2 and 3

present an estimate of Ψ_A and Ψ_O from, respectively, the NCEP–National Centers for Atmospheric Research (NCAR) reanalyses and a long simulation of an ocean circulation model. Application of these estimates to the partitioning problem will be presented in section 4. In section 5 we propose simple scalings to understand the mass transport and energy contrast limits highlighted above. Motivated by these simple arguments, in section 6 we analyze a coupled climate model of intermediate complexity run in an aquaplanet geometry. A partitioning very similar to the modern observational record is found, suggesting that it is likely to be a robust feature of the earth's climate. We summarize and conclude in section 7.

2. Atmospheric mass transport

a. *Meridional mass transport within moist static energy layers*

We use daily estimates of temperature T, geopotential Φ, and specific humidity q from the NCEP–NCAR reanalysis (Kalnay et al. 1996) on a 2.5° × 2.5° grid and 17 pressure levels. The central diagnostic variable is a quantity θ_A proportional to the moist static energy,[1] defined by the relation

$$C_A\theta_A \equiv C_A T + L_v q + \Phi, \tag{3}$$

where L_v is the latent heat of vaporization and C_A is the specific heat capacity of dry air. Figure 3 shows the zonal-mean distribution of θ_A (dashed contours), which can be compared to the dry potential temperature θ (continuous contours). The most striking feature is the homogeneity of θ_A in the Tropics, which is consistent with the tropical atmospheric lapse rate being close to that of a moist adiabat (Xu and Emanuel 1989). Another interesting tropical feature is the presence of a low to midlevel minimum of θ_A, associated with the subsidence of dry air from aloft. In midlatitudes, one observes that θ_A contours slope more steeply than θ contours due to the water vapor loading term in Eq. (3). Note that the shading in Fig. 3 indicates the zonal mean distribution of Ertel's potential vorticity (PV)—the 3-PV U contour (the dashed white line) will be used below to define the position of the tropopause [1 potential vorticity unit (PVU) = 10^{-6} K m^2 s^{-1} kg^{-1}].

On a given day, the meridional mass transport within an air column is partitioned into a set of θ_A layers with

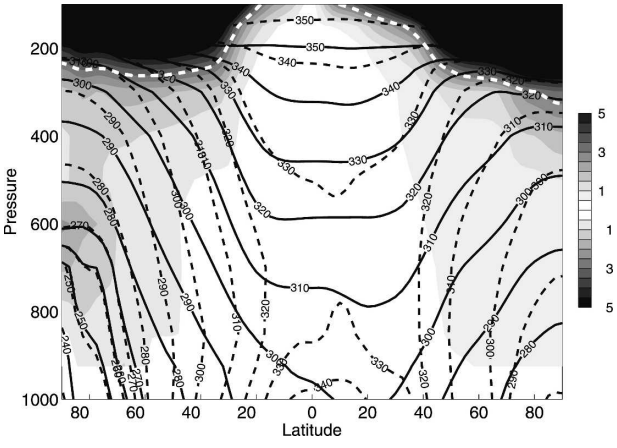

FIG. 3. Zonal mean distribution of θ_A (dashed contours) and θ (continuous contours) for the period from 1 May 2003 to 30 Sep 2003 (contour interval is 10 K). The zonal mean distribution of Ertel's PV, in PVU (1 PVU = 10^{-6} K m^2 s^{-1} kg^{-1}) is shaded. The tropopause (defined as the 3-PVU contour) is indicated by the thick dashed white line.

a resolution $\delta\theta_A$ = 5 K (finer θ_A grids were also considered but the results were found to be insensitive to this choice). For each θ_A layer the total meridional transport across a given latitude was then computed by summing the contributions over each longitude. Note that to enforce mass conservation, the long-term mean northward mass transport per temperature class (expressed in kg s^{-1} K^{-1} and hereafter denoted by M), summed over all temperature classes, was set to zero for each latitude. From M, at each latitude ϕ we compute a mass transport streamfunction Ψ_A (in kg s^{-1}) using the definition:

$$\Psi_A(\phi, \theta_A) = -\int_{\theta_A^{\min}}^{\theta_A} M(\phi,\theta'_A)\, d\theta'_A, \tag{4}$$

where we imposed that Ψ_A vanishes for all latitudes at a chosen low temperature $\theta_A^{\min}$. With the sign convention adopted, a positive Ψ_A indicates clockwise circulation in the (ϕ, θ_A) plane. An appendix sets out more details of the mass transport calculations.

Figure 4 shows our estimate of Ψ_A for the period of 1 May 2003 to 30 September 2003 (Fig. 4a; Southern Hemisphere winter) and for the period 1 November 2002 to 31 March 2003 (Fig. 4b; Northern Hemisphere winter). In the Southern Hemisphere, one observes a single equator-to-pole circulation in both seasons, with poleward mass transport at high θ_A and equatorward mass transport at low θ_A. The wintertime cell is the most intense, reaching a maximum of more than 200 Sv at a latitude of ~40°. Note that we have redefined a Sverdrup (the traditional oceanographer's unit of volume transport) to represent a mass transport (i.e., 1 Sv ≡ 10^9

[1] Note that θ_A as defined in Eq. (3) is related to, but not the same as, moist potential temperature. It is a measure of enthalpy rather than entropy.

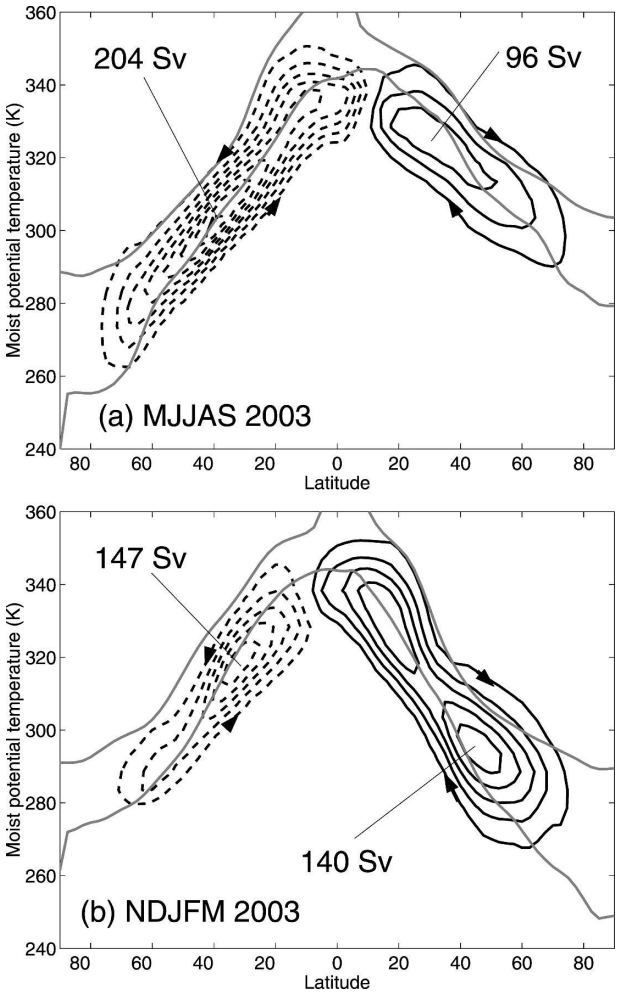

FIG. 4. Atmospheric meridional mass transport streamfunction within moist static energy layers (contoured every 25 Sv where 1 Sv = 10^9 kg s^{-1}; positive when clockwise, see arrows; zero contour omitted; extrema indicated on the plot) for (a) Southern and (b) Northern Hemisphere winter of 2003. The x axis denotes latitude and the y axis θ_A (K). The upper (lower) gray curve is the zonally average θ_A at the tropopause (ground).

kg s^{-1}).[2] In the Northern Hemisphere summer (Fig. 4a) we again observe a single equator-to-pole cell with a maximum of about 100 Sv near 30° of latitude. In winter, however, there is indication of two separate centers of action in Fig. 4b near 20° and 50° of latitude, each with an amplitude of about 140 Sv. We note that meridional mass transports of 100–200 Sv are significantly larger than the typical 20 Sv observed in the ocean. Below we suggest that this is indeed the major reason why the atmospheric contribution to H dominates over that of the ocean in mid-to-high latitudes.

In Fig. 4, we also plot (gray lower curve) the zonally averaged mean surface θ_A. It is readily seen that most of the equatorward mass transport occurs in layers with temperatures colder than the mean (zonally averaged) surface θ_A. In midlatitudes this is because [see Held and Schneider (1999)] the equatorward mass transport is achieved by cold air outbreaks, that is, transient features of the general circulation. In the Tropics however, there is a different reason: a picture very similar to Fig. 4 can be obtained (in the 20°S–20°N latitude band) if seasonal mean, rather than daily fields of meridional velocity and moist potential temperature are used (not shown). Equatorward mass transport at a lower θ_A than that of the (zonally averaged) θ_A at the ground occurs because of zonal asymmetries in the surface θ_A, the equatorward flow being found mostly at low levels over the cold tongues of the Atlantic and Pacific oceans (not shown).

The upper gray curve in Fig. 4 is the value of θ_A on the tropopause. It is seen that the latter gives a good estimate of the upper boundary of the cells for all seasons and both hemispheres.

b. Discussion of atmospheric mass transport

A striking result in the above analysis is that the Hadley and midlatitude eddy-driven cells tend to be joined in to a single cell (Figs. 4a,b). This is a pronounced feature of our diagnostics, even more so than in previous estimates of meridional mass transport streamfunction within dry potential temperature layers—the so-called residual circulation (e.g., Karoly et al. 1997; Held and Schneider 1999).

To understand the origin of this difference, we display in Fig. 5 the analog of Fig. 4 but for a calculation in which we have set $L_v = 0$ in (3), thereby only considering the contribution of dry static energy to the heat transport. One then observes a much more pronounced two cell structure in each winter hemisphere, with the tropical (Hadley) cell dominating. The differences between Figs. 4 and 5 can only arise because of moisture effects. They simply reflect that moisture and dry static energy are both transported poleward in mid-to-high latitudes, and so add to one another to create the vigorous overturning cell in midlatitudes seen in Fig. 4, while they oppose each other in the Tropics, thereby reducing the pronounced Hadley cell component in Fig. 4.

A second important aspect we wish to discuss is whether the midlatitude circulation in Figs. 4a,b can

[2] This choice is made for ready comparison to oceanic mass transports. The density of seawater is always close to 10^3 kg m^{-3}, so that a Sverdrup of 10^6 m^3 s^{-1} represents a mass transport of 10^9 kg s^{-1}. Accordingly, a mass transport of, say, 20×10^9 kg s^{-1} is the same as a volume transport of 20×10^6 m^3 s^{-1} in the ocean, i.e., "volume (Sv)" and "mass Sverdrups" are equivalent to one another.

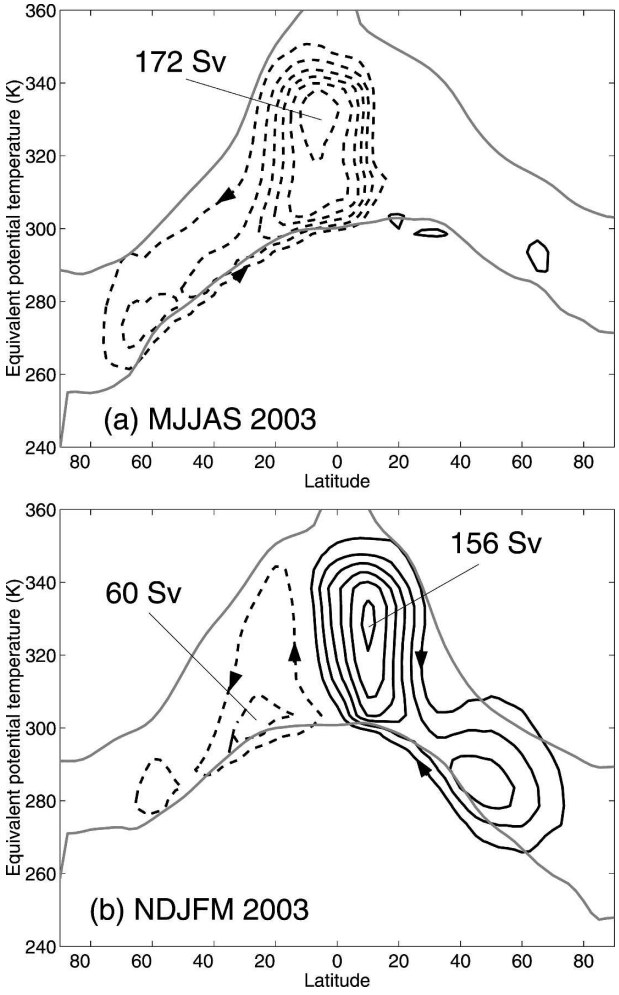

FIG. 5. Same as Fig. 4 but for the meridional mass streamfunction within dry static energy layers. The y axis now denotes an equivalent potential temperature computed as $C_A T + \Phi$.

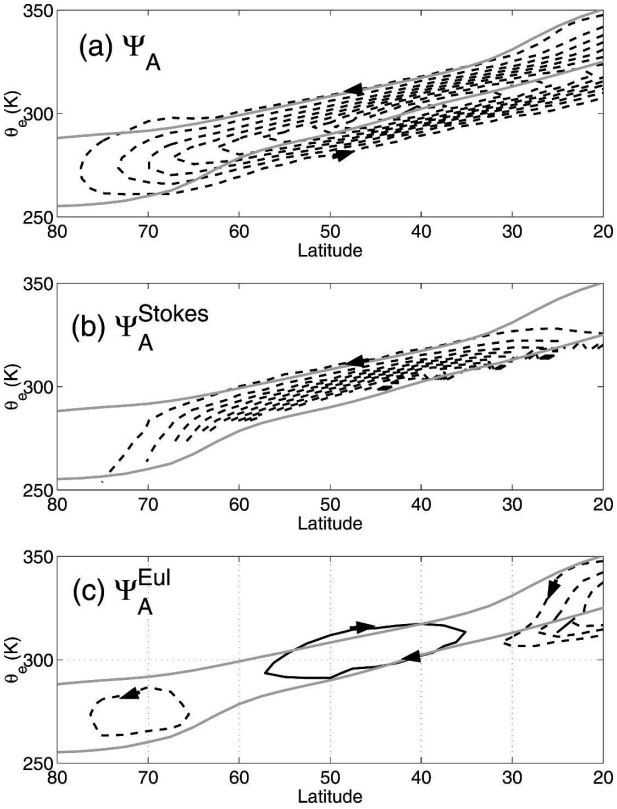

FIG. 6. Various estimates of the mass streamfunction within θ_A layers (a) direct, as in Fig. 4a, (b) using Eq. (6), and (c) the Eulerian mean. Contour interval is 20 Sv. Gray curves as in Fig. 4a.

indeed be interpreted as an overturning cell in the meridional-height plane. To address this issue, we check against observations that Ψ_A is well approximated by Ψ_A^{TEM}, the streamfunction advecting the zonal mean θ_A in a transformed Eulerian mean (TEM) formulation (Andrews et al. 1987). This is written as

$$\Psi_A \simeq \Psi_A^{\mathrm{TEM}} \equiv \Psi_A^{\mathrm{Eul}} + \Psi_A^{\mathrm{Stokes}}, \tag{5}$$

where Ψ_A^{Eul} is the Eulerian mean mass streamfunction and Ψ_A^{Stokes} is the quasi-Stokes mass streamfunction (e.g., Hoskins 1983) defined as

$$\Psi_A^{\mathrm{Stokes}} \equiv \frac{L_x}{g} \frac{\overline{v'\theta'_A}}{\partial \bar{\theta}_A / \partial p}. \tag{6}$$

In Eq. (6), L_x is the length of a latitude circle, g is gravity, p pressure, and $\overline{v'\theta'_A}$ is the meridional eddy flux of moist potential temperature (primes denote departures from zonal and time mean, denoted by an overbar).

Figure 6 compares Ψ_A from the direct calculation (Fig. 6a, reproduced from Fig. 4a) and an estimate of each term in the rhs of Eq. (5) for the Southern Hemisphere winter of 2003. Both the Eulerian (Fig. 6c) and the quasi-Stokes (Fig. 6b) streamfunctions were computed in the latitude–pressure plane, then mapped onto the latitude–θ_A plane using zonal mean, wintertime averaged θ_A profiles.[3] It is seen that in midlatitudes, the quasi-Stokes contribution alone is a very good description of the intensity and meridional/θ_A scales of Ψ_A (as before, gray curves indicate the θ_A of the tropopause and the ground). In midlatitudes, the Eulerian contri-

[3] Note that, for the Southern Hemisphere case considered in Fig. 6, only transient eddies were included in the computation of $\overline{v'\theta'_A}$ in (6). The contribution of steady eddies was found to be negligible except close to the Antarctic continent, where the contribution was noisy (not shown).

bution—the Ferrel cell—is a thermally indirect cell,[4] of much smaller intensity. As the Tropics is approached, however, the Eulerian contribution—the wintertime Hadley cell—dominates the total mass transport and provides a good approximation to Ψ_A.

That the approximation Eq. (5) holds gives support to the interpretation of Ψ_A as a true overturning cell in the meridional–height plane.[5] This interpretation can also be understood more physically by noting that Ψ_A^{Stokes} in Eq. (5) is an approximation to the Stokes drift associated with baroclinic waves (e.g., Wallace 1978).

3. Oceanic mass transport within θ layers

The oceanic analog to moist static energy is simply the internal energy, $C_O\theta_O$, where C_O is the specific heat capacity of seawater and θ_O is the potential temperature referenced to the surface [see Warren (1999) for a detailed discussion of how $C_O\theta_O$ approximates the oceanic total energy, i.e., the Bernoulli function, as defined, e.g., by Gill (1982)]. We therefore present an estimate of the meridional mass transport within potential temperature (θ_O) layers from a long simulation of the Massachusetts Institute of Technology (MIT) general circulation model (GCM; Marshall et al. 1997). The model is a state of the art GCM forced by seasonally varying surface winds and buoyancy forcing. It was run on the cubed sphere grid (Adcroft et al. 2004) at coarse resolution (15 vertical levels and C32 $\simeq 2.8° \times 2.8°$ in the horizontal). More information about the simulation can be found in the appendix.

From the last 50 yr of a thousand-year integration, we have estimated a time mean meridional velocity (v) and potential temperature field, as well as a time mean bolus velocity (v^*) introduced by the Gent and McWilliams scheme (Gent and McWilliams 1990). The latter is meant to represent the Stokes drift associated with baroclinic eddies (section 2b), which, unlike in the atmospheric calculations above, are not explicitly resolved in this coarse ocean model simulation. At each grid point, the water column is partitioned into a set of θ_O layers (with a resolution of $\delta\theta_O = 1$ K) and the meridional mass transport ($v + v^*$) within each layer is computed. Note that this procedure neglects time-dependent effects that, in this simulation, are limited to the seasonal cycle (no interannual variability in the surface forcing). The error thereby introduced in the annual mean was estimated by comparing the ocean heat transport computed from time mean $v + v^*$ and θ_O with that obtained from the time mean of the product $(v + v^*)\theta_O$. It was found to be negligible. Further details of the numerical procedure are discussed in the appendix.

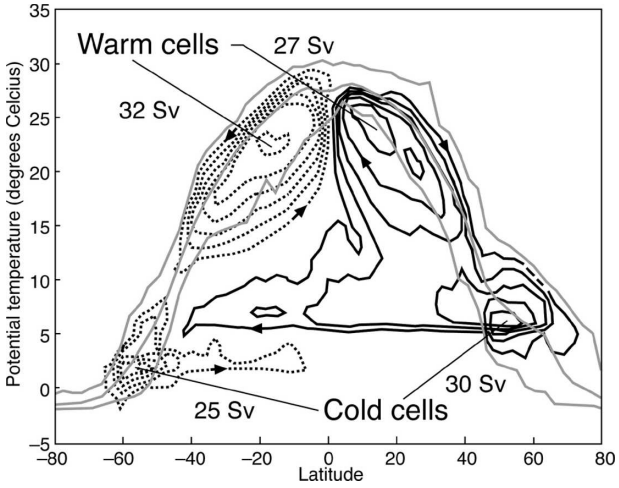

FIG. 7. Annual mean mass streamfunction in the ocean within θ_O layers (contoured every 5 Sv, continuous when clockwise; zero contour omitted). The x axis is latitude and the y axis potential temperature θ_0 (°C). The middle gray curve is the zonally average surface θ_O while the upper and lower gray curves indicate the maximum and minimum surface θ_O as a function of latitude.

Figure 7 shows the mass streamfunction within θ_O layers for the global ocean, calculated from Eq. (4) in the same way as in the atmosphere. One observes prominent cells at warm temperatures ($\theta_O = 15°$–30°C), flanked by cold ($\theta_O \leq 10$°C) deep cells at higher latitudes. The intensity of the warm and cold cells is comparable ($\simeq$30 Sv). The poleward flow in both cold and warm cells typically occurs at a temperature that is larger than the zonally average surface temperature (shown by the thick median gray curve in Fig. 7; the warmest and coldest surface temperature are also indicated as the upper and lower gray curves). This is the oceanic analog to the observation that in the atmosphere, equatorward flow occurs at a temperature lower than the surface owing to the effect of transient eddies (see section 2). In the ocean, it is a consequence of the three-dimensional character of the steady circulation depicted in Fig. 7, with advection in warm western boundary currents and their interior extension being a key aspect. As we will see below, Ψ_O differs from basin to basin. Overall, the features in Fig. 7 are significantly more complicated than its two-dimensional atmospheric counterpart in which there is a single overturning cell in each hemisphere, see Fig. 4.

Analysis of the mean thickness of the θ_O layers re-

[4] By thermally direct (indirect) we mean a meridional circulation with ascent where the fluid is warm (cold) and descent where it is cold (warm).

[5] The good agreement between Ψ_A and Ψ_A^{TEM} is not unexpected for those θ_A layers which do not intersect the ground (see McIntosh and McDougall 1996).

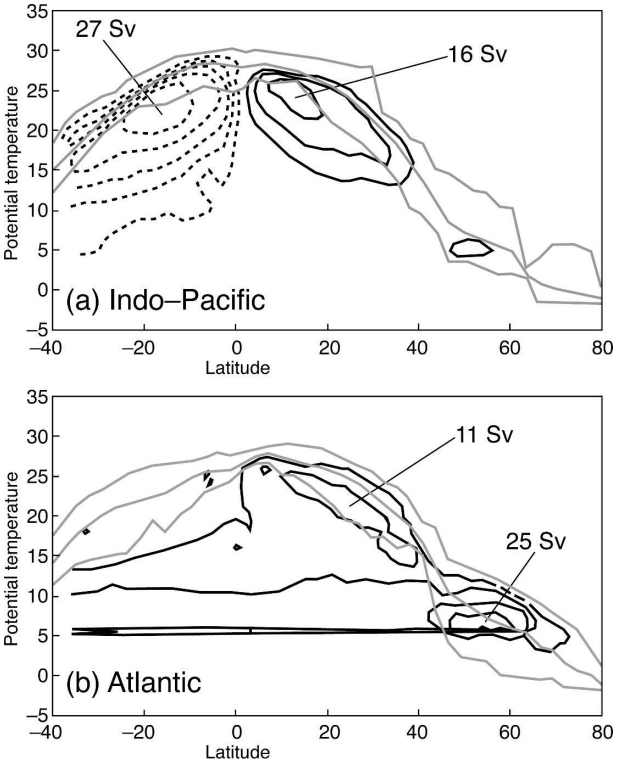

FIG. 8. Same as Fig. 7 but for the (a) Indo-Pacific and (b) Atlantic basins.

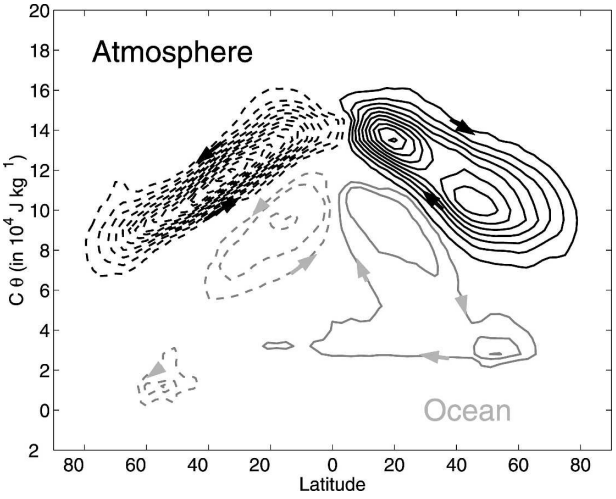

FIG. 9. Annual mean atmospheric (black) and oceanic (gray) mass streamfunction within constant energy layers. The contour interval is 10 Sv, dashed when circulating anticlockwise. The y axis is an energy coordinate ($C\theta$) in units of 10^4 J kg^{-1}. The oceanic cells are the same as shown in Fig. 7 (annual mean) while the atmospheric cells are an annual-mean estimate obtained by averaging Figs. 4a,b.

veals (not shown) that the warm cells occupy a volume of fluid with high stratification (thin layers) and can be identified with the mass circulation within the ventilated thermoclines of the Southern and Northern Hemispheres. This is further confirmed by the fact that their poleward extension is rather well predicted by the position of the midlatitude zero wind stress curl lines (not shown).

The cold cells are associated with thick θ_O layers (weak stratification) and correspond to the circulation of North Atlantic Deep Water and Antarctic Bottom Water. Note that the traditional Eulerian mass streamfunction displays more modest ($\simeq$10–15 Sv) cold cell mass transports.

Further information about Ψ_O is provided in Fig. 8, where the calculation was repeated separately for the Indo-Pacific (Fig. 8a) and Atlantic (Fig. 8b) basins. A simple partitioning is thereby obtained, in which the two warm (symmetric) cells originate in the main from the Indo-Pacific basin and the (asymmetric) Northern cold cell from the Atlantic basin.

4. The partitioning of heat transport

We now combine oceanic and atmospheric mass streamfunctions within their respective potential temperature layers. In so doing (Fig. 9), we have mapped the y axis of Figs. 4 and 7 on to an energy axis, which is $C_A\theta_A$ for the atmosphere and $C_O\theta_O$ for the ocean.

The first striking feature of Fig. 9 is that, as anticipated in section 2, the intensity of the oceanic cell is much weaker than its atmospheric counterpart (both are annual averages, see caption of Fig. 9). Even at 20°, where Ψ_O reaches its maximum, the atmospheric mass transport is roughly 4 times that of the ocean. It is only within the deep Tropics that the two transports are comparable. This is further demonstrated in Fig. 10 (continuous black curve), which shows the ratio of the maximum of Ψ_O and that of Ψ_A, computed from Fig. 9 at each latitude. Note that since both Ψ_O and Ψ_A become small close to the equator, the mass ratio shown in Fig. 10 is rather noisy at low latitudes.

The second important feature seen in Fig. 9 is that the thickness of the cells in energy space is comparable. To estimate this more precisely, we have used Fig. 9 and computed the change in $C_O\theta_O$ and $C_A\theta_A$ (hereafter denoted as $C_O\Delta\theta_O$ and $C_A\Delta\theta_A$, respectively) across a reference contour of mass transport. The latter was chosen to be 10% of the overall maximum of Ψ_O (0.1×32 Sv $\simeq 3$ Sv in the ocean) and Ψ_A (0.1×143 Sv $\simeq 14$ Sv in the atmosphere). The ratio $C_O\Delta\theta_O/C_A\Delta\theta_A$ is plotted in Fig. 10 (gray). As one approaches the Tropics, where $\Delta\theta_A$ is small, the ratio diverges. Conversely, on moving to high latitudes where oceanic potential temperature variations are small (weak stratification), the ratio approaches zero. In midlatitudes, $C_O\Delta\theta_O/C_A\Delta\theta_A$

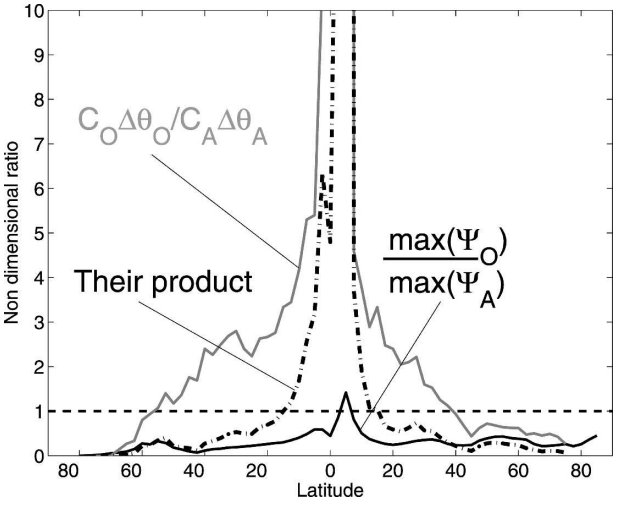

FIG. 10. The ratio $C_O\Delta\theta_O/C_A\Delta\theta_A$ (gray), max (Ψ_O)/max(Ψ_A) (continuous black), and their product (dot–dashed), computed from Fig. 9. A ratio of unity is indicated by the horizontal dashed line.

is of the order of unity, the differences in heat capacity ($C_O/C_A \simeq 4$) being compensated for by a larger temperature difference across the atmospheric cell ($\Delta\theta_A \simeq$ 40 K compared to $\Delta\theta_O \simeq 10$ K).

The product of the continuous black (Ψ ratio) and gray ($C\Delta\theta$ ratio) curves allows an estimate of the respective contribution of mass transport and energy contrast to the partitioning of heat transport. It is shown as the black dot–dashed line in Fig. 10, and falls between the black and gray curves. Indeed, the energy contrast tends to favor the ocean as the major contributor to the total heat transport up to latitudes of 40°–50°. However, the mass transport strongly favors the atmosphere as the dominant contributor to the total heat transport at almost all latitudes. The net result of these two competing effects (dot–dashed curve) is consistent with the partitioning shown in Fig. 1b, with the atmosphere dominating the total heat transport for latitudes poleward of about 20°.

Finally, we briefly comment on the interpretation of the $C\Delta\theta$ term as a measure of stratification. As can be seen from Fig. 4, in both the Tropics and midlatitudes, $C_A\Delta\theta_A$, the typical change in moist static energy across Ψ_A, is significantly different (twice as large) from the tropopause to ground θ_A difference. Similarly in the ocean, it is readily seen from Fig. 7 that $C_O\Delta\theta_O$ for the warm cells is significantly different (by about 20%–30%) than a (zonally averaged) surface to thermocline bottom temperature difference. One must be careful, then, when estimating the energy contrast across the oceanic and atmospheric circulations appropriate for computation of meridional energy transport.

5. Scalings

Our diagnostics suggest that the observed ratio H_A/H_O, which is larger (smaller) than unity poleward (equatorward) of roughly 30°, can be understood as a consequence of two simple limits of Eq. (2):

(i) dominance of atmospheric mass transport in mid-to-high latitudes ($\Psi_A \gg \Psi_O$ with $C_A\Delta\theta_A \sim C_O\Delta\theta_O$ and hence $H_A/H_O \gg 1$)
(ii) dominance of oceanic energy contrast in the Tropics ($C_O\Delta\theta_O \gg C_A\Delta\theta_A$ with $\Psi_A \sim \Psi_O$ and hence $H_A/H_O \ll 1$)

The second limit—also invoked by Held (2001)—is the easiest to rationalize since it simply invokes small energy contrasts within the tropical atmosphere (and roughly equivalent mass transports, see introduction). This is a consequence of deep convection returning the atmosphere to a moist adiabatic lapse rate and dynamical adjustments smoothing out significant horizontal potential temperature gradients within ±15° of the equator. On the other hand, the predominance of atmospheric over oceanic meridional mass transport in midlatitudes [limit (i)] is perhaps somewhat counterintuitive in view of the much larger density of water compared to air. We now attempt to understand $\Psi_A \gg \Psi_O$ using dynamical scalings.

Our starting point is to view the mass circulations Ψ_A and Ψ_O as overturning cells in the meridional–height plane. This simplification is justified by Fig. 6 for the atmosphere, in which the quasi-Stokes advection provides a good description of Ψ_A in midlatitudes (see section 2b). It is probably less so in the ocean because of a more fundamental three-dimensional circulation that contributes to Ψ_O (see section 3). Nevertheless we will limit ourselves to this simple picture. For such an overturning circulation, a simple estimate of the mass transport is given by (appropriate to both ocean and atmosphere)

$$\Psi = \rho\Delta z V L = \frac{\Delta_z P}{g} V L, \tag{7}$$

where ρ is the density, V is a typical meridional velocity, Δz is the vertical scale of the overturning, and L is the zonal length scale over which the circulation extends, and the hydrostatic relation has been used. All terms are estimated for either the poleward or the equatorward branch of the circulation. Since the ocean has a much greater density than the atmosphere, the $\Delta_z P/g$ term in Eq. (7) will always be larger for an oceanic cell. On the other hand, meridional velocities tend to be much larger in the atmosphere than in the ocean. Since zonal lengths L are of similar magnitude in both ocean

and atmosphere, there must be a strong compensation of mass and velocity effects. This suggests that a simple scaling based on (7) will be problematical since it must account for two large, compensating terms.

To overcome this problem, we focus directly on the mass transport streamfunctions Ψ_A and Ψ_O and within a quasigeostrophic framework propose a simultaneous treatment of their dynamics. For the ocean, we will consider both the case of a channel geometry (with meridional overturning cell but no gyres) and that of a basin geometry with meridional boundaries (both gyres and overturning cell).

Let us consider, then, the zonally averaged zonal momentum balance for the ocean or the atmosphere, modeled as Boussinesq fluids in a Cartesian geometry (neglecting advection of mean momentum by the mean flow),

$$-f\bar{v} = -\frac{\Lambda}{\rho_{\rm ref}}\frac{\partial \bar{p}}{\partial x} - \frac{\overline{\partial u'v'}}{\partial y} + \frac{1}{\rho_{\rm ref}}\frac{\partial \bar{\tau}}{\partial z}. \tag{8}$$

Here, x, y, and z denote longitude, latitude, and height, respectively, f is the Coriolis parameter, p the pressure, u and v denote the zonal and meridional velocities, ρ_{ref} is a reference density, and τ represent the turbulent stress due to small-scale processes. As in (6), primes denote departures from the zonal and time mean (indicated by an overbar). The parameter Λ is set to unity for the case of the ocean with basin geometry, acknowledging the presence of east–west pressure gradients across latitude circles, and anticipating the results presented in section 6, it is set to zero in the case of an ocean channel geometry and in the atmospheric case.[6] Following the standard transformed Eulerian mean procedure (e.g., Andrews et al. 1987; Marshall and Radko 2003), we rewrite (8) as

$$-f\bar{v}_{\rm res} = f\frac{1}{\rho_{\rm ref}}\frac{\psi_{\rm res}}{\partial z} = -\frac{\Lambda}{\rho_{\rm ref}}\frac{\partial \bar{p}}{\partial x} - \frac{\overline{\partial u'v'}}{\partial y} + \frac{1}{\rho_{\rm ref}}\left[\frac{\partial \bar{\tau}}{\partial z} + \frac{\partial \tau_{\rm eddy}}{\partial z}\right], \tag{9}$$

where $\bar{v}_{\rm res}$, $\psi_{\rm res}$ are the residual mean meridional velocity and mass streamfunction, respectively ($\psi_{\rm res} > 0$ is clockwise in the latitude–height plane, i.e., representing a thermally direct circulation in the Northern Hemisphere), and $\tau_{\rm eddy}$ is the associated eddy stress given by

$$\tau_{\rm eddy} = \rho_{\rm ref} f \frac{\overline{v'\theta'}}{d\theta/dz}, \tag{10}$$

[6] This neglects form drag at the lowest oceanic and atmospheric levels.

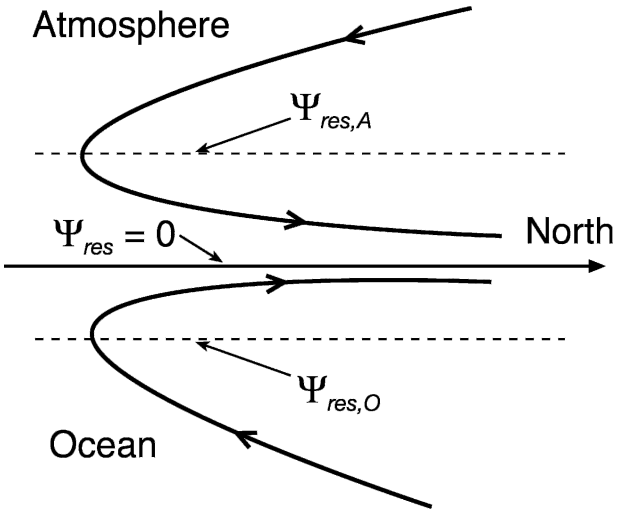

FIG. 11. Schematic of the residual circulation $\psi_{\rm res}$ in the atmosphere and the ocean in an aquaplanet geometry such as the Southern Ocean. At the surface, $\psi_{\rm res}$ vanishes in both ocean and atmosphere, while along the horizontal dashed line it reaches a maximum value in the interior of the respective fluids. This maximum is denoted by $\psi_{{\rm res},A}$ (atmosphere) and $\psi_{{\rm res},O}$ (ocean). Equation (9) is integrated over the oceanic and atmospheric layers bounded by the surface and the dashed line.

where $d\theta/dz$ is a reference potential temperature gradient. Note the connection of (10) with the Stokes streamfunction defined in (6).

In the atmosphere we integrate Eq. (9) with $\Lambda = 0$ in the vertical from the sea surface (where $\psi_{\rm res} = 0$ and $\bar{\tau} = \tau_s$, the zonal surface wind stress, positive for midlatitude westerlies) to the level where the residual mean streamfunction is a maximum and $\bar{\tau} = 0$ (Fig. 11). A further simplification arises because over this bottom layer the Reynolds stress term in (9) can be safely neglected. Denoting by $\psi_{{\rm res},A}$ the interior maximum of $\psi_{\rm res}$ (where the eddy stress is τ_A), we obtain

$$\psi_{{\rm res},A} \simeq \frac{\tau_A - \tau_s}{f}. \tag{11}$$

Since typically $\tau_A \gg \tau_s$—see further discussion below—, this equation shows that baroclinic eddies tend to drive a thermally direct circulation (τ_A, $\psi_{{\rm res},A} > 0$ in the Northern Hemisphere) opposed by a thermally indirect Ekman (or Ferrell) cell associated with surface wind stress.

In the ocean we integrate vertically over the upper layer of the meridional circulation, from the depth $-D$ where $\psi_{\rm res}$ reaches its maximum (denoted by $\psi_{{\rm res},O}$; see Fig. 11) and the turbulent stress $\bar{\tau}$ vanishes at the sea surface where again $\psi_{\rm res} = 0$ and $\bar{\tau} = \tau_s$. Even though currents, and hence Reynolds momentum fluxes, are the largest in this layer; even here, Reynolds stresses

can be neglected compared to the eddy stress τ_{eddy}, owing to the small Rossby number in the ocean. Integration of (9) thus yields

$$\psi_{\text{res},O} \simeq \frac{\tau_O - \tau_s}{f} + \frac{\Lambda}{f}\int_{-D}^{0} \Delta_x \overline{p} dz, \tag{12}$$

which includes a contribution from zonal pressure gradient $d\overline{p}/\partial x$, which we have rewritten as $\Delta_x \overline{p}$, in the case of a basin geometry ($\Lambda = 1$). In the latter case, we must relate $\Delta_x \overline{p}$ to other variables. This is done, following Marshall (1997), by considering the vertically averaged (from surface to bottom depth $-H$) zonal momentum balance of the ocean. From Eq. (8) with $\Lambda = 1$, neglecting bottom turbulent stresses and again Reynolds momentum stresses, we have

$$-f\int_{-H}^{0} \overline{v}\, dz = 0 = -\frac{1}{\rho_{\text{ref}}}\int_{-H}^{0} \Delta_x \overline{p} dz + \frac{\tau_s}{\rho_{\text{ref}}}, \tag{13}$$

which yields

$$\int_{-H}^{0} \Delta_x \overline{p} dz = \tau_s. \tag{14}$$

A simple closure is now chosen in which we assume that the zonal pressure gradient integrated over the upper layer of the residual flow is proportional to the depth-averaged zonal pressure gradient, thus,

$$\int_{-D}^{0} \Delta_x \overline{p}\, dz = a\int_{-H}^{0} \Delta_x \overline{p} dz = a\tau_s, \tag{15}$$

where a is a (nondimensional) constant of proportionality and we have used (14). Making use of Eq. (15) in (12), we finally obtain

$$\psi_{\text{res},O} \simeq \frac{\tau_O - (1 - a\Lambda)\tau_s}{f}. \tag{16}$$

Just as in its atmospheric counterpart [Eq. (11)], Eq. (16) indicates that eddy stresses tend to drive a thermally direct circulation. Unlike the atmosphere, however, the presence of meridional boundaries ($\Lambda \neq 0$) introduces a pressure gradient term, which partly compensates the zonal wind stress forcing. Equations (11) and (16) suggest a scaling of the ratio of atmospheric to oceanic mass transport streamfunction, thus,

$$\frac{\Psi_A}{\Psi_O} \propto \frac{\psi_{\text{res},A}}{\psi_{\text{res},O}} \simeq \frac{\tau_A - \tau_s}{\tau_O - (1 - a\Lambda)\tau_s}. \tag{17}$$

In the case of purely axisymmetric dynamics (no eddies, $\tau_A = \tau_O = 0$, and $\Lambda = 0$), the ratio of atmospheric to oceanic mass transport is $\Psi_A/\Psi_O = 1$. The sense of circulation and mass transport of the atmospheric and oceanic cells is the same (the Ekman mass transport), as in Held's (2001) discussion of the coupled tropical circulation. In midlatitudes, however, the eddy stresses cannot be neglected, and the ratio Ψ_A/Ψ_O depends on their strength relative to the surface wind stress.

Inspection of Fig. 6 suggests that, in the atmosphere in midlatitudes, the Stokes streamfunction (see section 2b) is much larger (by at least a factor of 2) than the Eulerian (Ferrell) circulation ($\tau_A \gg \tau_s$) and Eq. (17) reduces to

$$\frac{\Psi_A}{\Psi_O} \simeq \frac{\tau_A}{\tau_O - (1 - a\Lambda)\tau_s}. \tag{18}$$

In the Southern Ocean, characterized by a channel geometry ($\Lambda = 0$), diagnostic and theoretical studies suggest that the sense of the residual circulation is set by the wind (the so-called Deacon cell, $\psi_O \propto -\tau_s/f$ with an equatorward upper level flow), although its magnitude can be significantly reduced by the presence of the eddy stress term τ_O (Karsten and Marshall 2002; Marshall and Radko 2003; Olbers et al. 2004). In a basin geometry ($\Lambda = 1$), such as occurs in the North Atlantic Ocean, the upper flow is poleward in midlatitudes, that is, opposite to the direct Ekman flow driven by the surface westerlies. Eddy stresses and, even more likely, zonal pressure gradients across the basin must thus dominate Eq. (16). Indeed, about 15 Sv of water is believed to flow poleward at upper levels in the North Atlantic (Ganachaud and Wunsch 2000) while over the same basin the Ekman contribution is about 5 Sv equatorward in midlatitudes.[7] Neglecting τ_O in (16), this requires $a \simeq 4$. Such a value reflects the large baroclinic structure of the pressure field, yielding larger upper level pressure gradients than depth-averaged ones, see Eq. (15).

In summary, the mass transport in the atmosphere in midlatitudes is driven by baroclinic eddies and is associated with a thermally direct circulation. The surface westerlies produce an Ekman transport opposing the eddy-driven mass flux. This situation is somewhat analogous to the ocean in a channel geometry where cancellation exists between eddy- and wind-driven meridional mass transports, with the important difference that surface westerlies are driven by atmospheric eddies whereas oceanic eddies are a consequence of the surface wind through its role in generating potential energy (Gill et al. 1974). These different causal relationships probably explain why in the atmosphere the eddy-driven mass flux dominates over Ekman, while the

[7] This is assuming $\tau_s = 0.1$ N m^{-2}, $f = 10^{-4}$ s^{-1}, and a zonal length scale of 5000 km.

reverse situation occurs in the Southern Ocean. The presence of meridional boundaries may dramatically change the state of affairs, as it allows the large-scale geostrophic flow to add constructively to the eddy driven flow and contribute to a net thermally direct overturning circulation, as observed in the North Atlantic.

Overall, the above discussion suggests that, in midlatitudes, the sign of Ψ_A/Ψ_O is probably dependent upon the geometry (negative in a channel where surface flows can be in the same direction in both the atmosphere and ocean, see Fig. 11; positive in a basin, with opposite direction of surface flows, see Fig. 9), but that its amplitude is primarily controlled by the ratio of atmospheric eddy stress to surface wind stress, assuming that $|\tau_O - (1 - a\Lambda)\tau_s| \simeq \tau_s$. We thus obtain the following scaling for the ratio of mass transport as

$$\left|\frac{\Psi_A}{\Psi_O}\right| \simeq \frac{\tau_A}{\tau_s}. \tag{19}$$

This ratio appears as the key parameter of our study. Since surface wind stress balances the vertically integrated eddy fluxes of zonal momentum, τ_A/τ_s can be thought of as a measure of the importance of eddy heat fluxes [see Eq. (10)] versus momentum fluxes, that is, of the relative strength of the vertical and horizontal components of the Eliassen–Palm flux (e.g., Edmon et al. 1980). It is unclear to us whether or not there is anything fundamental about a ratio $\tau_A/\tau_s > 1$, associated with most of the wave activity propagating upward and being dissipated in place (vertical Eliassen–Palm flux limit).

6. Partitioning in a coupled climate model

The scalings proposed in the previous section are rather basic in the sense that they do not rely on a detailed representation of geometry and orography, etc. One thus expects that the heat transport partitioning seen in the observations should also be found in the presence of very different continental configurations. We now briefly explore this possibility by analyzing the partitioning of heat transport in a long simulation of a coupled model of intermediate complexity run in the absence of continents (aquaplanet geometry) but with an active dynamical ocean.

The coupled model consists of a five-layer primitive equation atmosphere with simplified physical representations (Molteni 2003), coupled to the MIT ocean model as described in Marshall et al. (2004). The atmosphere and ocean are run on the same cubed sphere grid (see Adcroft et al. 2004) at a horizontal resolution of C32 ($\simeq 2.8° \times 2.8°$). The ocean bottom is flat with a constant depth of 5200 m. A linear bottom drag is applied to the lowest oceanic layers to control the model barotropic mode. The coupled system also includes a simple thermodynamic sea ice model based on Winton (2000). The results presented below are based on the last 500 yr of a 1500-yr integration.

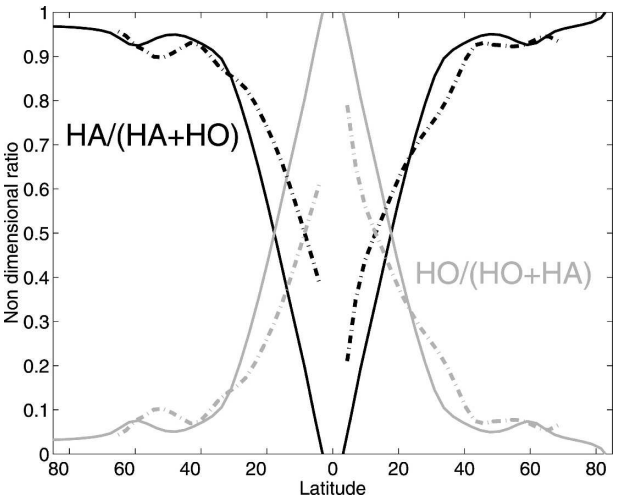

FIG. 12. As in Fig. 1b but for the coupled model in an aquaplanet geometry (continuous curves). As a reference, observed ratios are also indicated (broken curves). The latter were computed from the observations presented in Fig. 1a, averaging the NCEP and ECMWF oceanic and atmospheric heat transports.

Figure 12 displays the contribution of the atmosphere (black) and the ocean (gray) to the total heat transport (H_A/H and H_O/H, respectively) in the aquaplanet coupled model in a format similar to Fig. 1b. One observes (continuous curves) that again a simple partitioning is found, with the atmosphere dominating poleward of 20° and the ocean dominating equatorward of 20°. For reference, we have also indicated the corresponding curves from observations (see caption of Fig. 12) as broken black and gray curves. The similarity between the two sets of curves is striking. Even in a world very different from our own, the partitioning of heat transport between the atmosphere and ocean remains, to first order, the same.

Further diagnostics indicate that this similarity can again be explained from the two limits invoked in section 5. The oceanic energy contrasts are large in the Tropics where equatorial upwelling creates a sharp, strong thermocline, whereas moist static energy contrasts are extremely weak in the model tropical atmosphere, even more so than in the real world owing to the absence of zonal SST gradients associated with the cold tongue and the absence of land–sea contrasts in the aquaplanet geometry. The atmospheric mass transport peaks at about 30° with a value $\simeq$200 Sv while the

oceanic mass transport peaks at 20° with a value of ≃60 Sv, leading the atmosphere to be the main carrier of energy poleward of 20°.

7. Summary and conclusions

A diagnostic study of the partitioning of the total poleward heat transport between the ocean and atmosphere was presented in a coordinate system comprising latitude and energy. In this coordinate system, the poleward heat transport by both the ocean or the atmosphere scales as $H = \Psi C\Delta\theta$, where Ψ represents the meridional mass transport within θ layers (moist static energy or moist potential temperature for the atmosphere, potential temperature for the ocean) and $C\Delta\theta$ scales the energy difference across the circulation defined by Ψ.

Both the oceanic (Ψ_O) and atmospheric (Ψ_A) meridional mass transports are remarkable. In the atmosphere, a single equator-to-pole cell appears in each hemisphere, a feature highlighted in previous studies of the residual circulation, but which is even more pronounced here where moist, rather than dry, potential temperature is used. The oceanic streamfunction shows a distinct hemispheric asymmetry in both warm wind-driven cells and cold buoyancy-driven cells.

Two simple limits emerge from our diagnostics. In mid-to-high latitudes, the intensity of the atmospheric meridional mass transport dominates that of the ocean ($\Psi_A \simeq 100$ Sv compared to $\Psi_O \leq 30$ Sv). With such a dominant mass transport, here the atmosphere is the main contributor to the total poleward heat transport ($H_A/H_O \simeq \Psi_A/\Psi_O \gg 1$). In the Tropics however, $\Psi_A/\Psi_O \simeq 1$, energy contrast sets the partitioning and the ocean becomes the major contributor to the total poleward heat transport ($H_A/H_O \simeq C_A\Delta\theta_A/C_O\Delta\theta_O \ll 1$).

We have argued that these two limits reflect fundamental, robust dynamics of the ocean–atmosphere system. The dominance of the atmospheric meridional mass transport in midlatitudes is a consequence of the efficiency of baroclinic eddies in driving a thermally direct circulation. The strength of the latter is more than twice that of the (indirect) Eulerian mean circulation (the Ferrel cell), which roughly scales the ocean meridional mass transport. The tendency of the atmosphere to be close to neutrality with respect to moist processes within 15° or so of the equator is chiefly responsible for the second limit.

As a consequence of these basic ideas, we have further argued that the observed partitioning is a robust feature of the earth's climate, unlikely to change significantly in a different configuration of continents, as has happened on geological time scales. Some support for this claim was obtained from a long simulation of an intermediate complexity climate model run in an aquaplanet geometry (no continents at all!).

Combined with the study of Stone (1978), who argued that the total (ocean + atmosphere) heat transport is essentially set by the planetary albedo, the solar constant and the radius of the Earth, our results suggest that the oceanic and atmospheric heat transport might themselves change rather modestly in very different climate states. In other words, climate variability may be associated with only small departures from fixed background H_A, H_O curves. This hypothesis does not rule out the possibility, known as Bjerknes' compensation idea (Bjerknes 1964), that changes in H_A and H_O oppose each other on long time scales. Our study suggests that such compensated changes may modify the partitioning by only a small amount, with the atmosphere continuing to dominate the total heat transport poleward of 20° and the ocean in the deep Tropics. These ideas will undoubtedly soon become testable as oceanic and atmospheric reanalyses products improve, and a vast hierarchy of coupled ocean–atmosphere models, in various geometries, become available for analysis.

Acknowledgments. This work was supported by a grant from NOAA's Office of Global Programs as part of Atlantic CLIVAR. Jean-Michel Campin was of tremendous help in analyzing the result of the ocean GCM. We would also like to thank the three reviewers for their helpful comments.

APPENDIX

Specific Details of the Mass Transport Calculation within θ Classes

a. Atmosphere

Daily outputs from the NCEP–NCAR reanalysis (Kalnay et al. 1996) were used to compute moist potential temperature θ_A and meridional velocity v at each nominal pressure level. First, on a given day, θ_A and v were interpolated onto a finer, regular ($\delta P = 10$ mb) pressure grid, in order to provide a better resolution in temperature class. Layers with pressure greater than the surface pressure for that day (the latter also being taken from the NCEP–NCAR reanalysis) were excluded from the calculation since they physically would lie below the ground. The meridional mass transport within the finer grid column ($v\delta P/g$ for a given pressure layer, where g is gravity) was subsequently repartioned as a function of moist potential temperature class, with

a resolution of $\delta\theta_A = 5$ K. Finer and coarser resolutions were tested for the Southern Hemisphere winter period of 2003 and found to produce very similar results. We thus used this resolution for all calculations presented here, including meridional mass transport within dry potential temperature layers.

b. Ocean

We use yearly outputs from a thousand-year-long integration of the MIT ocean GCM (Marshall et al. 1997) run on the cube sphere in z-level coordinates (Adcroft et al. 2004) with a realistic geometry. The model was forced by a seasonally varying climatology of surface wind stress and net surface heat flux and evaporation minus precipitation (the simulation is the same as that discussed in Marshall et al. 2004). The model has no surface mixed layer but a simple convective adjustment scheme. Surface temperature and salinity are restored to observed climatology with a time scale of 2 months and 2 yr, respectively. There is no sea ice model, but the temperature is maintained above freezing. A vertical diffusivity of $K_\upsilon = 3.10^{-5}$ m^2 s^{-1} was used for temperature and salinity. The Gent and McWilliams (1990) scheme is used together with an isopycnal diffusion (Redi tensor formalism) coefficient set to $K_\rho = 800$ m^2 s^{-1}.

The procedure to obtain the meridional mass transport within a set of θ_O (potential temperature) layers is almost identical to that used for the atmosphere (replacing the finer pressure grid by a finer geometric height grid with $\delta z = 10$ m). Only one change was made: since the ocean model predicts a transport within each layer, υ was kept the same when interpolating onto the finer z grid (yielding a staircaselike profile, as in the raw model outputs). This procedure exactly preserves the (vertically integrated) meridional mass transport at each grid point, but only approximately conserves the (vertically integrated) θ_O transport at each grid point. The error in the latter was found to never exceed 1%, however.

Finally, we emphasize that in both the ocean or atmosphere, the mass transport streamfunction Ψ computed from the meridional mass transport within θ layers according to Eq. (4) is different from the mass circulation within θ layers, that is, the diabatic circulation (e.g., Townsend and Johnson 1985). Estimating the latter would require the calculation of both meridional and upward mass flux within a set of θ layers, whereas we only considered the meridional mass flux. One must therefore be cautious when interpreting the cross θ flows in Figs. 4, 5, 7, and 8 as truly diabatic in origin.

REFERENCES

Adcroft, A. J., J.-M. Campin, C. N. Hill, and J. C. Marshall, 2004: Implementation of an atmosphere–ocean general circulation model on the expanded spherical cube. *Mon. Wea. Rev.,* **132,** 2845–2863.

Andrews, D. G., J. R. Holton, and C. B. Leovy, 1987: *Middle Atmosphere Dynamics.* International Geophysics Series, Vol. 40, Academic Press, 489 pp.

Bjerknes, J., 1964. Atlantic air–sea interaction. *Advances in Geophysics,* Vol. 10, Academic Press, 1–82.

Edmon, H. J., B. J. Hoskins, and M. E. McIntyre, 1980: Eliassen–Palm cross sections for the troposphere. *J. Atmos. Sci.,* **37,** 2600–2616.

Ganachaud, A., and C. Wunsch, 2000: Improved estimates of global ocean circulation, heat transport and mixing from hydrographic data. *Nature,* **408,** 453–456.

Gent, P. R., and J. C. McWilliams, 1990: Isopycnal mixing in ocean circulation models. *J. Phys. Oceanogr.,* **20,** 150–155.

Gill, A. E., 1982: *Atmosphere–Ocean Dynamics*. Academic Press, 662 pp.

——, J. S. A. Green, and A. J. Simmons, 1974: Energy partition in the large scale ocean circulation and the production of mid-ocean eddies. *Deep-Sea Res.,* **21,** 499–528.

Held, I. M., 2001: The partitioning of the poleward energy transport between the tropical ocean and atmosphere. *J. Atmos. Sci.,* **58,** 943–948.

——, and T. Schneider, 1999: The surface branch of the zonally averaged mass transport circulation in the troposphere. *J. Atmos. Sci.,* **56,** 1688–1697.

Hoskins, B. J., 1983. Modelling of the transient eddies and their feedback on the mean flow. *Large Scale Dynamical Processes in the Atmosphere,* R. P. Pearce and B. J. Hoskins, Eds., Academic Press, 160–199.

Kalnay, E., and Coauthors, 1996: The NCEP/NCAR 40-Year Reanalysis Project. *Bull. Amer. Meteor. Soc.,* **77,** 437–471.

Karoly, D. J., P. C. McIntosh, P. Berrisford, T. J. McDougall, and A. C. Hirst, 1997: Similarities of the Deacon cell in the Southern Ocean and Ferrel cells in the atmosphere. *Quart. J. Roy. Meteor. Soc.,* **123,** 519–526.

Karsten, R. H., and J. C. Marshall, 2002: Constructing the residual circulation of the Antarctic Circumpolar Current from observations. *J. Phys. Oceanogr.,* **32,** 3315–3327.

Marshall, D., 1997: Subduction of water masses in an eddying ocean. *J. Mar. Res.,* **55,** 201–222.

Marshall, J. C., and T. Radko, 2003: Residual mean solutions for the Antarctic Circumpolar Current and its associated overturning circulation. *J. Phys. Oceanogr.,* **33,** 2341–2354.

——, A. J. Adcroft, C. Hill, L. Perelman, and C. Heisey, 1997: A finite-volume, incompressible Navier Stokes model for studies of the ocean on parallel computers. *J. Geophys. Res.,* **102,** 5753–5766.

——, ——, J.-M. Campin, and C. Hill, 2004: Atmosphere–ocean modeling exploiting fluid isomorphisms. *Mon. Wea. Rev.,* **132,** 2882–2894.

McIntosh, P. C., and T. J. McDougall, 1996: Isopycnal averaging and the residual mean circulation. *J. Phys. Oceanogr.,* **26,** 1655–1660.

Molteni, F., 2003: Atmospheric simulations using a GCM with simplified physical parametrizations. I: Model climatology and variability in multi-decadal experiments. *Climate Dyn.,* **20,** 175–191.

Olbers, D., D. Borowski, C. Voelker, and J.-O. Wolff, 2004: The dynamical balance, transport and circulation of the Antarctic Circumpolar Current. *Antarct. Sci*., **16**, 439–470.

Stone, P. H., 1978: Constraints on dynamical transport of energy on a spherical planet. *Dyn. Atmos. Oceans,* **2,** 123–139.

Talley, L. D., 2003: Shallow, intermediate, and deep overturning components of the global heat budget. *J. Phys. Oceanogr.,* **33,** 530–560.

Townsend, R. D., and D. R. Johnson, 1985: A diagnostic study of the insentropic zonally averaged mass circulation during the first GARP global experiment. *J. Atmos. Sci.,* **42,** 1565–1579.

Trenberth, K. E., and J. M. Caron, 2001: Estimates of meridional atmosphere and ocean heat transports. *J. Climate,* **14,** 3433–3443.

Wallace, J. M., 1978: Trajectory slopes, counter gradient heat fluxes and mixing by lower stratospheric waves. *J. Atmos. Sci.,* **35,** 554–558.

Warren, B., 1999: Approximating the energy transport across oceanic sections. *J. Geophys. Res.,* **104,** 7915–7919.

Winton, M., 2000: A reformulated three-layer sea ice model. *J. Atmos. Oceanic Technol.,* **17,** 525–531.

Xu, K.-M., and K. A. Emanuel, 1989: Is the tropical atmosphere conditionally unstable? *Mon. Wea. Rev.,* **117,** 1471–1479.